CFD Analysis of the Effect of Temperature and Buoyancy Due to Concrete Building Structures Based from an Integrated DEM and Landsat Infrared Image

Manuel J Garcia, Pierre Boulanger*, Juan Duque, Santiago Giraldo

EAFIT University, Cr 49 No 7 sur 50, Medellin Colombia,
*University of Alberta, 2-21 Athabasca Hall, T6G 2E8, Canada

Abstract

The present paper deals with the influence of concrete structures on atmospheric temperature and the convection winds generated in the Aburra valley of Medelln, Colombia. This area is characterized by low wind velocities with a high industry density. A digital elevation model was used from the Radar Shuttle Topography Mission and post-processed in order to obtain a valid volumetric CFD domain. The construction process include hole filling due to imperfections in the original radar data, decimation of original cloud of points to reduce the excess of detail at regions with low curvature, and the introduction of a volume of air over the terrain surface (CFD domain). Landsat satellite data was used to set the terrain temperatures due to various material composition of the terrain. The converted infrared image was then registered into the CFD domain through an interpolation process.

Navier-Stokes Equations were solved for buoyant, turbulent flow of compressible fluid accounting for convection and heat transfer effects. Simulation includes buoyancy and turbulence flow through the k-epsilon model using the high performance computing facilities of Westgrid (Western Canada Research Grid). Preliminary results shows wind distributions that compares to the one observed in low altitude in the region.

1 Introduction

Wind standards and codes of practice typically assume a terrain of homogeneous roughness or provide explicit corrections for specific topographies such as hills or escarpments. For more complex situations they refer the practitioner to boundary layer wind tunnel tests. With the fast evolution of computers and algorithms, numerical low altitude wind simulation has become very attractive as it provides a low-cost alternative to evaluate wind effects.

This paper presents and discusses a methodology for numerical evaluation of buoyancy effects over complex terrain topographies. Computational domain is obtained by use of digital elevation models which allows automatic reconstruction of any terrain surface over the earth. Solution is obtained by solving the Navier-Stokes equations using the OpenFOAM (Open source Field Operation and Manipulation) toolkit using the high performance computing facilities of Westgrid[1].

This particular application is particularly useful for areas surrounded by mountains like valleys with no large wind speed due to the mountain protection. Applications include atmospheric heating and dispersion of pollutants in such areas. These model could help predict how contaminants disperse and reach populated areas. CFD simulation could provide a way to relocate factories near cities to minimize pollution effects Monti and Leuzzi (2005); Dawson et al. (1991); A et al. (2002); Kim et al. (2005).

2 Digital Elevation Models

Digital Elevation Models (DEM) are representations of elevation data of the earth's surface. They are organized in several files which contain latitude, longitude, and elevation coordinates of points over the earth's surface. One of the most complete collections of high-resolution DEM was acquired by the Shuttle Radar Topography Mission (SRTM) (NGA and NASA (2000)). Measurements were collected during a single eleven-day Endeavor Space Shuttle mission, STS–99, in February 2000 using a synthetic aperture radar. Topographic data was collected for dry lands (excluding water masses) between 56 degrees latitude South and 60 degrees latitude North, covering about eighty per cent of the total land of the earth.

The data gathered during the mission was processed and organized in two ways: a) Square segments covering one degree latitude by one degree longitude. Every segment was saved in a distinct file. Every file is organized as a grid of n rows and m columns of samples whose distance is either one arc second (1/3600 of degree) for the United

[1] Western Canada Research Grid

States (SRMT) or three arc seconds (SRMT3), for the rest of the world. b) Processed data can also be retrieved through the Seamless Data Distribution System (SDDS) of the US Geological Survey (USGS) and the EROS Data Center (EDC) service (2003). The main feature is that the user can define an area of interest by drawing a box, defining coordinates, or using available templates to cut out the area. They also offer a variety of DEM formats. One arc second measured at the equator, corresponds approximately to thirty meters, so two sampling points in a STRM3 file are roughly ninety meters from each other. This approximation will deteriorate as one move away from the equator in the direction of either poles.

Every sample is represented with a sixteen bit signed integer, row ordered. Integer coding is *big endian*, meaning that the first byte read is the most significant and the second is the least significant. The number associated with each sample corresponds to its elevation measured in meters with respect to the WGS84 EGM96 geoid. (The geoid is a rotational solid used in geodesy that approximates the shape of the earth better than a sphere or an ellipsoid.) Data files are not perfect and some *voids* are present. They are due to shadow or water reflexions creating distortions. Samples corresponding to these voids are given a conventional value of -32768 in the NASA files and 0 in the SDDS files.

3 Digital Terrain Thermal Distribution Using Landsat Infrared Imagery

The observation of the Earth by Landsat satellite and the imagery obtained from such missions goes back more than three decades ago, since 1972. Through MSS and Thematic Mapper(TM)image data has been acquired to set a unprecedented record of Earth's surface coverage within spatial scales of 30 and 80 m. TM sensors were included in Landsat missions 4 (1982 -1993) and 5(1984 - present), but MSS sensors have been on board from mission 1 through 5.

The global coverage obtained by the US of MSS and TM data has only been interrupted during the failure of the Ku-band transmitter, which led to the loss of access during this years to the Tracking and Data Relay Satellite System. Using data from international ground stations some of this gaps have been filled. The US began acquiring data once again with the launch of Landsat-7 Enhanced Thematic Mapper Plus (ETM+) in 1999, which included solid-state recorders.

On april 15 of 1999, the satellite mission LANDSAT-7 was launched with the objective of acquiring well calibrated data about the current status of earth's landscapesScaramuzza et al. (2004). The Enhanced Thematic Mapper plus (ETM+) used during this mission, provides results of 30 meters spaced data in six consecutive spectral bands(named respectively 1st -5th and 7th band), 15-m data in one panchromatic band (named PAN 8th band) and finally, one thermal band (6th Band). See Table for the respective wavelengths and the number of sensors associated to each bandOffice (2002).

Band	**Wavelength (nm)**	**Spacing(m)**
1^{st}	$[441 - 514]$	30
2^{nd}	$[519 - 601]$	30
3^{rd}	$[631 - 692]$	30
4^{th}	$[772 - 898]$	30
5^{th}	$[1547 - 1748]$	30
7^{th}	$[2064 - 2346]$	30
$PAN(8^{th})$	$[515 - 896]$	15
$Thermal(6^{th})$	$[10440 - 12420]$	60

All data obtained on each band is acquired in one or two gain states of the instrument and mapped into a eight bit code. For more information regarding the Landsat missions and instruments, see Office (2002).

Top Of Atmosphere (TOA) radiances are measured with Thermal Infra-Red (TIR) sensors of the satellite, this radiances are transformed into brightness temperatures (or black body temperatures) using Planck's law Dash et al. (2002). The combination of the emitted radiance from the Earth's surface, the upward radiance from the atmosphere and the downward radiance from the sky sum together to deliver the TOA radiances. Depending on the atmospheric conditions land surface brightness and TOA temperatures differ within a 1 to 5 $°K$ range in the 10-12 μm spectral region Prata et al. (1995). Corrections of atmospheric effects, like absorption, upward emission, and downward irradiance reflected from the surface must be done before obtaining land surface brightness temperatures Franca and Cracknell (1994). To obtain a more accurate LST, roughness properties of the land surface, the amount and nature of vegetation cover, and the thermal properties and moisture content of the soil must be accounted for by correcting brightness temperatures using spectral emissivity values before computation occurs Friedl (2002).

3.1 Creation of a CFD Domain from DEM Data

CFD domains are created from the DEM information and should cover a large enough portion to guarantee accuracy in the simulation. For wind simulation a volume of air over the surface constitutes the CFD domain.

3.2 Void Management

Data from the SRMT should be completed to generate the domain. Voids can be filled in different ways which include several interpolation techniques. Also, information from other sources like other DEM databases or GPS measurements can be used to complete the data. A simple interpolation technique uses information from the closest points around a void $\vec{x}$,

$$z(\vec{x}) = \frac{1}{n} \sum_{\vec{q}_j \in \Omega_x}^{n} w_j \, z(\vec{q}_j), \;\; \Omega_x = \left\{ \vec{q}_j \;\middle|\; \quad ||\vec{x} - \vec{q}_j|| < r \right\}, \tag{1}$$

with w_j a weight factor and $r \in \mathbb{R}$. The disadvantage of this is that due to the nature of the holes (they can be large along one direction) it could result in a good approximation in one direction and a deficient approximation of the slope and curvature in the other direction. This weighted average can be further enhanced if a least square approximation is taken over a patch $||\vec{x} - \vec{q}|| < r$ around a void García (1999). However, it is the shape of the patch that it should be consider. Thus the following interpolation takes the weighted average of the closest points different to zero (valid points) in all directions (North, East, West, South). The weight is the inverse of the distance, and therefore the closest points have the largest weight. The weight equation is,

$$z(\vec{x}) = \left(\frac{1}{\sum_j w_j} \right) \sum_{j \in \Omega} w_j z(\vec{q}_j) \tag{2}$$

with $w_j = \left({}^{1}\!\middle/\!{}_{||\vec{x} - \vec{q}_j||} \right)$ and $\Omega_x = \vec{q}_j$ such that $\min ||\vec{x} - \vec{q}_j||$, for each $\vec{q}_j$ taken in the North, East, South, and West directions and $z(\vec{q}_j) \neq 0$

3.3 Mesh Generation

The finished DEM data is transformed into a regular grid of triangular elements, e.g., a two-manifold with border that represents the terrain surface. SRMT data files cover an approximate area of 108×108 km. As SRMT3 data is sampled at every three arc sec it will contains in total $1,442,401$ equidistant points. This surface can be efficiently decimated preserving the curvature detail by suppressing points at low curvature regions. Depending on the topography of the terrain it can be reduced up to fifteen per cent or even ten per cent of the original data while keeping the approximation error low.

CFD domain consist of a volume of air over the terrain surface. It can be generated by projecting vertical walls along the sampled terrain boundary

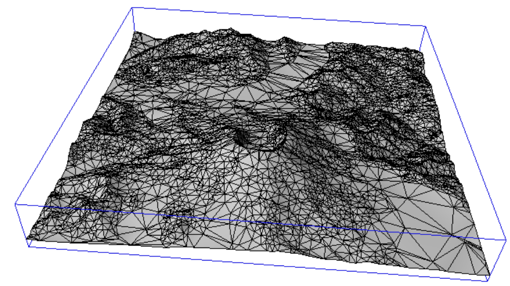

(a) Terrain surface after decimation

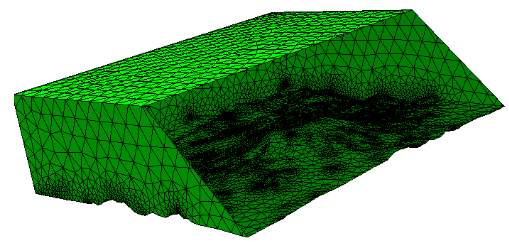

(b) Cut of the CFD domain over the terrain surface

Figure 1: Superficial mesh and domain for CFD analysis.

and then intersecting the resulting shell with a horizontal plane at a given height h. The final manifold must be closed and topologically correct (See figure 1).

Once a correct superficial mesh of the domain is obtained, a volumetric mesh is generated. An ideal mesh for the volume element method consists of hexahedral elements. However, this is difficult to obtain automatically and there are several research groups working on this problem. An alternative to hexahedral meshes are the so called unstructured tetrahedral meshes. They should be used with caution when implementing the volume element method and orthogonal correctors should be used to assure convergence. In this study tetrahedral meshes are generated using NETGEN (Schberl, 2005). The NETGEN algorithm can be summarized as follows: It starts from either a CAD model or a superficial mesh in STL format that should be topologically correct. NETGEN starts by computing the corner points and edges that are meshed into segments and the faces are meshed by an advancing front surface mesh generator. Faces meshes are optimized to obtain a good quality superficial mesh. The domain is filled with tetrahedra volumetric elements using a fast Delaunay algorithm. This generates most of the elements but it often fails to complete the whole domain. Then, a slower backtracking rule-based algorithm takes over and completes the task. As a final step the volumetric mesh is optimized by the standard node-movement, element swapping, and splitting algorithms (Schberl, 2005).

Mesh grading towards the terrain is not necessary when using the standard $k-\epsilon$ model with wall functions since the flow in the near wall cell is modelled, rather than having to be resolved. Nevertheless, due to the size of the domain, a moderate grading is maintained in order to reduce the mesh size.

4 Setting Boundary Conditions

Due to the boxed shape of the domain, boundary surfaces are: the terrain surface, the south, north, east and west walls, and the top surface.

The main goal was to simulate the wind creation by buoyancy effects due to the heating of the terrain by solar radiation.

4.1 Conversion of Landsat Data into Surface Temperature

Two approaches to recover LST from multi-spectral TIR imagery have been developed Schmugge et al. (1998). One corrects the at-sensor radiance to surface radiance using a radiative transfer equation, later temperature and emissivity are obtained from surface radiance applying an emissivity model Schmugge et al. (1998). The other approach uses a split-window technique for sea surfaces to land surfaces and assumes that emissivity in the channels used for the split window is similar Dash et al. (2002). Then with a linear combination of the two channels surface brightness temperatures are calculated. The most noticeable disadvantage of this method is that the coefficients are only valid for the data sets from which they were derived Dash et al. (2002). This means that extrapolation of a set of thermal responses for a process or a specific landscape phenomenon measured using a specific TIR sensor is not possible, and TIR measurements from other sensors or from images recorded at different times using this same sensor cannot be predicted.

4.1.1 Derivation of Land Surface Temperature from Landsat ETM+ imagery

Using the corrected ETM+ TIR band (10440-12420 nm) LST were derived.To convert the Digital Number (DN) ranging from 0-255 of the Landsat ETM+ TIR band into spectral radiance, the following equation was used Office (2002):

$$L_\lambda = 0.0370588 \times DN + 3.2 \tag{3}$$

Assuming uniform emissivity, the satellite brightness temperature (Black-body Temperature, T_B) can be obtained converting the spectral radiance Office (2002). The formula used for the conversion is:

$$T_B = \frac{K_2}{\ln\left(\frac{K_1}{L_\lambda} + 1\right)} \tag{4}$$

where T_B is effective at-satellite temperature in $^\circ K$, L_k is the spectral radiance in $W/(m^2 sternm)$; as well,$K_2 = 1282.71^\circ K$ and $K_1 = 666.09 mW*cm^{-2}*sr^{-1}*\mu m^{-1}$ are taken as pre-launch calibration constants for Landsat-7 ETM+ missionOffice (2002).

Since the temperature values obtained previously are referenced to a black body, corrections for spectral emissivity (ϵ) depending on the nature of land cover became necessary.The land surface temperatures (St) that already have been corrected with emissivity were computed as followsArtis and Carnahan (1982):

$$S_T = \frac{T_B}{1 + \left(\lambda + \frac{T_B}{\rho}\right) \ln \varepsilon} \tag{5}$$

where: λ is the wavelength of the emitted radiance (taking for this case a value of (λ =11500 nm) as the peak response and the average of the limiting wavelengths), β =Boltzmann constant (1.38*10^{-23}J/K), ρ =h*c/β = (1.438*10^{-2}m$^\circ K$), h = Planck's constant (6.626*10^{-34} Js),and c = velocity of light (2.998*10^8 m/s). Using the near-infrared (0.76-0.90 μm) and visible (0.63-0.69μm) bands of the ETM+ image the NDVI image was computed, bringing forth a new possible set of studies for the relationship between LST and NDVI.

Other boundary conditions include,

- uniform initial velocity of $\vec{u} = (0, 0, 0)$ m/s;
- outlet (with fixed pressure $p = 0$ Pa;
- no-slip walls over the terrain;
- wall functions over the terrain;
- temperature mapped over the terrain;
- temperature symmetry conditions over the side walls $\nabla \vec{T} \cdot \hat{n} = 0$;
- initial internal pressure of 1 atmosphere and velocity 0 m/s;
- wall buoyant pressure over the walls

5 Buoyancy Model

Buoyancy effects is simulated using the OpenFoam toolkit. OpenFOAM is the Open Source Field Operation and Manipulation (OpenFOAM) C++ library used primarily to create applications (Weller et al., 1998; Jasak et al., 2004).

The governing equations are: The mass continuity

$$\frac{\partial \rho}{\partial t} + \nabla \cdot (\rho \vec{u}) = 0. \tag{6}$$

The Momentum equation

$$\frac{\partial \rho \vec{u}}{\partial t} + \nabla \cdot (\rho \vec{u} \vec{u}) = \nabla \cdot (\mu \nabla \vec{u}) - \nabla p + (\rho - \rho_0)\vec{g} + S_v. \tag{7}$$

Where $(\rho - \rho_0)\vec{g}$ is the buoyancy term and ρ_0 is the reference density. In the $k - \varepsilon$ model two extra

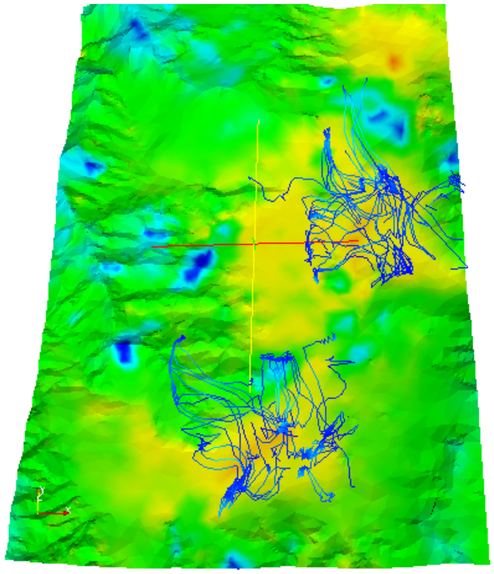

(a) Top view

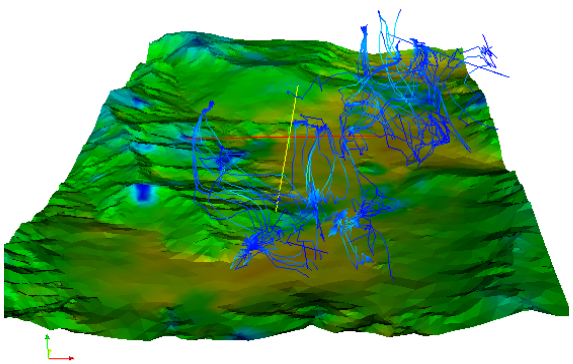

(b) Front-top view.

Figure 2: Terrain temperature and stream lines after 400 s. Emissivity of the terrain was taken constant at a value of 1.

equations are needed for the closure. The transport equation for k is,

$$\frac{\partial(\rho k)}{\partial t} + \nabla \cdot (\rho \vec{u} k) = \nabla \cdot (\Gamma_k \nabla k) + P + B - \rho\varepsilon, \tag{8}$$

where P is the usual production or generation term and G is the generation term due to buoyancy and is given by

$$B = \beta g_i \frac{\mu}{\sigma_T}\frac{\partial T}{\partial x_i}, \qquad \text{with} \qquad \beta = -\frac{1}{\rho}\frac{\partial \rho}{\partial T},$$

the coefficient of volumetric expansion. The transport equations for ε is

$$\frac{\partial(\rho\varepsilon)}{\partial t} + \nabla \cdot (\rho \vec{u}\varepsilon) = \nabla \cdot (\Gamma_\varepsilon \nabla \varepsilon) + \frac{\varepsilon}{k}\left(C_{\varepsilon 1}(P+G)(1+C_3 R_f) - C_{\varepsilon 2}\rho\varepsilon\right) \tag{9}$$

where R_f is the flux Richardson number and C_3 is an additional model constant (Rodi, 1980). Also a brief summary of the buoyancy model can be found in Versteeg and Malalasekera (1995).

The constants of the turbulence model are empirically determined and taken for the $k-\varepsilon$ model Ferziger and Perić (2002) as, $C_\mu = 0.09$; $C_1 = 1.44$; $C_2 = 1.92$; $\sigma_k = 1$; $\sigma_\epsilon = 0.76923$.

To guarantee convergence of the solution an initial field is needed. It can be obtained by solving for potential flow φ over the domain by

$$\nabla^2\varphi = 0 \tag{10}$$

and solving for $\vec{u}$ from

$$\mathrm{grad}\,\varphi = \vec{u}. \tag{11}$$

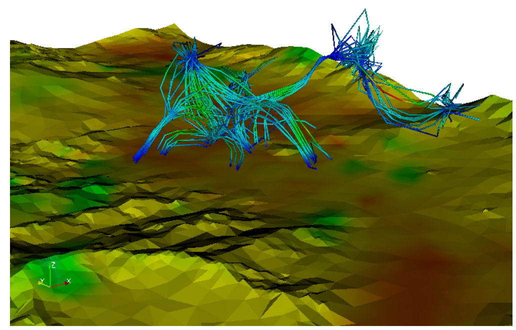

(a) Top view

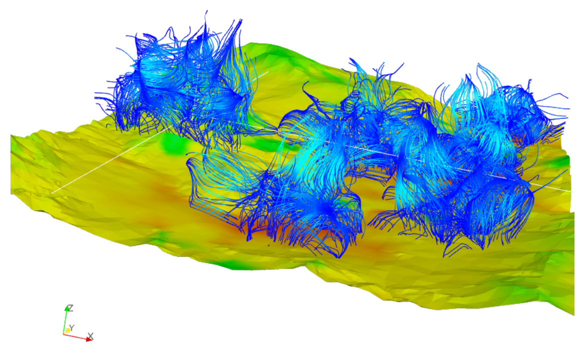

(b) Front-top view.

Figure 3: Terrain temperature and stream lines after 400 s. Emissivity equal to 0.8

6 The Aburra's valley

A rectangular subset of the Aburra valley was analyzed. The coordinates of the lower-left point of the area are 425 000 East and 678 000 North WGS84 UTM datum 18. In Geographic Coordinates it corresponds to -75° 40' 40.241" West and 6° 8' 0.2943" North. The size of the rectangular area is 15660 m (West-East) by 24480 m (South-North). DEM data with the same coordinates was selected from the SDDS site. The minimum height of the terrain is 1408 m and the maximum height 3 138 m over sea level. A volume of air with a height of 6 000 m over the valley was taken as the CFD domain. Temperature were computed from Landsat data using the method described previously and interpolated to fit with the terrain coordinates. In this particular case the temperature was computed using a emissivity of one which results in temperatures in between 6.2 to 24.5°C over the surface. Figure 2 shows two different view with the temperature map over the surface and some stream lines over the hottest points. This hottest points correspond to highly constructed areas with very low green and high percentage of industrial plants. The stream lines correspond to the 400 s simulation time step. the maximum velocity produced after this time was 0.02 m/s. Solution time was 74.49 hours with a single processor and 14 hours with eight processors.

Figure 3 shows stream lines for the same terrain but with an emissivity of 0.8. Minimum and maximum temperatures were 20.9° C and 41° C which can be typical of a very hot day in the area. Visualization of the stream lines shows that the air recirculation is larger than in the previous case.

7 Conclusions

Wind simulation is being increasingly studied over the past decades. High Performance Computation (HPC) has made more accurate simulations possible in a reasonable time-frame. There are still some problems to be addressed as a the lack of highly accurate terrain models, mesh generation, automatic processing, and also accurate solvers that include all the physical phenomenons relevant to a wind simulation scenario.

The availability of digital elevation models DEM from the Shuttle Radar Topography Mission allows accurate and automatic composition of CFD domains for wind simulations. The scheme proposed here uses a tetrahedral mesh that in spite of its automatic advantages, is not optimum when using the Finite Volume Method. Further research needs to be done in the direction of automatic hexahedral generators for complex topographic terrains.

Assessment of the temperature of the terrain accomplished through band 6 of Landsat 7, which is recognized as the temperature band. This is computed from equations with two different emissivities. Thus producing two different temperature maps over the region. However emissivities are a function of the terrain material and this it is not accounted in the present study. They can be computed from the other bands in the Landsat data. The effect however can be predicted as lower temperatures in the green area and higher temperatures in the built area, thus increasing the temperature gradient and favoring the buoyancy effects.

References

Walton A, Cheng A.Y.S., and Yeung W.C. Large-eddy simulation of pollution dispersion in an urban street canyon-part i: comparison with field data. *Atmospheric Environment*, 36(22):3601–3613, 2002.

D.A. Artis and W. H. Carnahan. Survey of emissivity variability in thermography of urban areas. *Remote Sensing of Environment*, 12:313–329, 1982.

R. Benoit, M. Desgagne, P. Pellerin, S. Pellerin, Y. Chartier, and S. Desjardins. The canadian mc2: A semi-lagrangian, semi-implicit wideband atmospheric model suited for finescale process studies and simulation. *Mon. Wea. Rev.*, 125: 23822415, 1997.

G. T Bitsuamlak, T. Stathopoulos, F. ASCE, and C B. Numerical evaluation of wind flow over complex terrain: Review. *Journal of Arospace Engineering*, 17(4):135–144, Octubre October 2004.

P. Dash, F.-M. Gottsche, F.-S. Olesen, and H. Fischer. Land surface temperature and emissivity estimation from passive sensor data:theory and practice-current trends. *International Journal of RemoteSensing*, 23(13):2563–2594, 2002.

Paul Dawson, David E. Stock, and Brian Lamb. The numerical simulation of airflow and dispersion in three-dimensional atmospheric recirculation zones. *Journal of Applied Meteorology*, 30 (7):1005–1024, 1991.

J. H. Ferziger and M. Perić. *Computational Methods for Fluid Dynamics.* Springer, 3rd edition, 2002.

G. B. Franca and A. P. Cracknell. Retrieval of land and sea surface temperature using noaa-11 avhrr data in north-eastern brazil. *International Journal of Remote Sensing*, 15:1695–1712, 1994.

M. A. Friedl. Forward and inverse modeling of land surface energy balance using surface temperature measurements. *Remote Sensing of Environment*, 79:344–354, 2002.

Manuel J. García. *Fixed Grid Finite Element Analysis in Structural Design and Optimization.* PhD. Thesis The University of Sydney, Sydney, 1999.

H. Jasak, H.G. Weller, and N. Nordin. In-cylinder CFD simulation using a C++ object-oriented toolkit. SAE Technical Paper 2004-01-0110, 2004.

Si-Wan Kim, Chin-Hoh Moeng, Jeffrey C. Weil, and Mary C. Barth. Lagrangian particle dispersion modeling of the fumigation process using large-eddy simulation. *Journal of athmosferic Sciences*, 62(6):1932–1946, 2005.

A. Leonard. Energy cascade in large eddy simmulations of turbulent fluid flow. *Adv. Geophys.*, 18A: 237, 1974.

Paolo Monti and Giovanni Leuzzi. Development of numerical model for dispersion over complicated terrain in the convective boundary layer. *International Journal of Environment and Pollution*, 25(1-4):239–250, 2005.

NGA and NASA. The shuttle radar topography mission (srtm). `http://www2.jpl.nasa.gov/srtm/`, 2000.

Landsat Project Science Office. *Landsat 7 Science Data Users Handbook*. Goddard Space Flight Center, NASA, Washinghton, 2002.

Jean-Paul Pinard, Robert Benoit, and Wei Yu. A WEST wind climate simulation of the mountainous yukon. *Atmosphere-ocean*, 43(3):259282, 2005.

A. J. Prata, V. C. Coll, J.A Sobrino, and C. Ottle. Thermal remote sensing of land surface temperature from satellites: Current status and future prospects. *Remote Sensing Reviews*, 12:175–224, 1995.

W. Rodi. Turbulence models and their application in hydraulics - A state of the art review. *NASA STI/Recon Technical Report A*, 81:21395–+, December 1980.

Pat L. Scaramuzza, Brian L. Markham, Julia A. Barsi, and Ed Kaita. Landsat-7 etm+ on-orbit reflective-band radiometric characterization. *IEEE Transactions on geoscience and remote sensing*, 42(12), December 2004.

T. Schmugge, S. J. Hook, and C. Coll. Recovering surface temperature and emissivity from thermal infrared multispectral data. *Remote Sensing of Environment*, 65:121–131, 1998.

Joachim Schberl. *NETGEN*. Johannes Kepler University Linz., Austria, 4.3 edition, 2005. `http://www.hpfem.jku.at/netgen`.

US. Geological service. Seamless data distribution system. `http://seamless.usgs.gov/`, 2003.

H. K. Versteeg and W. Malalasekera. *An Introduction to Computational Fluid Dynamics*. Prentice Hall, Essex, 1995.

J. Walmsley, D. Woolridge, and J. Salmon. Ms-micro/3 user's guide, 1990.

H.G. Weller, G. Tabor, H. Jasak, and C. Fureby. A tensorial approach to computational continuum mechanics using object orientated techniques. *Computers in Physics*, 12(6):620 – 631, 1998.